

Article

High Accuracy Modeling of Permanent Magnet Synchronous Motors Using Finite Element Analysis

Hanaa Elsherbiny ^{1,*} , Laszlo Szamel ² , Mohamed Kamal Ahmed ¹ and Mahmoud A. Elwany ¹¹ Electrical Engineering Department, El-Azhar University, Cairo 11651, Egypt² Department of Electric Power Engineering, Faculty of Electrical Engineering and Informatics, Budapest University of Technology and Economics, 1111 Budapest, Hungary

* Correspondence: hanaaelsherbiny.60@azhar.edu.eg

Abstract: Permanent magnet synchronous machines (PMSMs) have garnered increasing interest because of their advantages such as high efficiency, high power density, wide speed range, and fast dynamics. They have been employed recently in several industrial applications including robotics and electric vehicles (EVs). However, PMSMs have highly nonlinear magnetic characteristics, especially interior PMSMs, due to the existence of reluctance torque. Nonlinearity complicates not only machine modeling but also control algorithms. An accurate machine model is the key aspect for the prediction of machine performance as well as the development of a high-performance control algorithm. Hence, this paper presents an accurate modelling method for PMSMs. The proposed model method is applicable for all PMSMs, even multiphase machines. This paper considers a fractional slot concentrated winding 12/10 interior PMSM (IPMSM) for this study to demonstrate the effect of magnetic saturation and special harmonics. The developed model considers accurately the magnetic saturation, mutual coupling, spatial harmonics, and iron loss effects. It utilizes finite element analysis (FEA) to estimate the precise magnetic characteristics of IPMSM. The finite element model is calibrated precisely using experimental measurements. The iron losses are estimated within the simulation model as d- and q-axes current components. The model accuracy is validated experimentally based on a 12/10 IPMSM prototype.

Keywords: permanent magnet synchronous machine; finite element analysis; calibration; magnetic saturation; spatial harmonics; iron losses

MSC: 37M05; 00A72; 93-10



Citation: Elsherbiny, H.; Szamel, L.; Ahmed, M.K.; Elwany, M.A. High Accuracy Modeling of Permanent Magnet Synchronous Motors Using Finite Element Analysis. *Mathematics* **2022**, *10*, 3880. <https://doi.org/10.3390/math10203880>

Academic Editors: Vladimir Prakht and Anton Dianov

Received: 9 September 2022

Accepted: 16 October 2022

Published: 19 October 2022

Publisher's Note: MDPI stays neutral with regard to jurisdictional claims in published maps and institutional affiliations.



Copyright: © 2022 by the authors. Licensee MDPI, Basel, Switzerland. This article is an open access article distributed under the terms and conditions of the Creative Commons Attribution (CC BY) license (<https://creativecommons.org/licenses/by/4.0/>).

1. Introduction

Because of their superiorities permanent magnet synchronous machines (PMSMs) have garnered increasing interest. They have high efficiency, high power density, a wide range of operating speeds, small size and weight, and low noise [1–3]. Recently, interior PMSMs (IPMSMs) showed the best overall performance for electric vehicles (EVs) [4,5]. IPMSMs can easily fulfil vehicle requirements with proper torque control [6,7]. However, IPMSMs are well known for their nonlinearity and torque ripple due to their magnetic saturation, spatial harmonics, and reluctance torque [8].

Developing and optimizing different control strategies of IPMSMs for high performance drives rely basically on modelling accuracy. The conventional machine models (CMMs) were introduced using fixed machine parameters regardless of the effects of saturation, spatial harmonics, and iron loss. These models cannot represent accurately the behavior of IPMSMs [3]. They can be used for initial machine designs. Therefore, several research studies have been done involving the production of high-fidelity machine models. The circuit-field coupled co-simulation is presented in [9–11]. This technique is very time-consuming due to the involvement of numerical finite element (FE). In [12], the

relationship between flux linkage and currents are fitted to be used within the simulation in order to avoid the FE computation in simulation. However, the fitting is a very complicated and time-consuming process. In [13], the modelling in the abc-reference frame is introduced using N-dimensional look-up tables (LUTs). The abc-model allows one to include both geometry and saturation-induced space harmonics naturally. The abc-model can provide relatively high accuracies, while the complex expressions are circumvented. In [14], conventional shallow neural networks (CSNN) are applied to fit torque–current characteristics. Due to the high nonlinearity of torque–current characteristics as well as the limited capability of CSNN to fit complex nonlinear systems, the torque and the significant harmonics cannot be accurately modelled. To consider the torque nonlinearity and the spatial harmonics, deep neural network are developed in [15]. However, the training of intelligent techniques requires high skills and a large number of given data. Moreover, measured samples are required to train the network or generate the rules.

Considerable interest has been given to the analytical models for IPMSMs. Modelling and quantifying the source of torque ripple as part of the dq-model are proposed in [16]. In [17,18], accurate estimation of average torque, including nonlinearity effects, is presented. In [8], with the consideration of magnetic saturation, spatial harmonics, cross-coupling, and temperature effects, the torque and the voltage equations are derived. However, these analytical models are very complicated for real-time implementation. In [19], an indirect analytical method is presented for V-shaped IPMSM. It transfers the rotor into an equivalent linear one in a polar coordinate system to analyze the magnetic field and predict cogging torque. However, a considerable error is obtained in predicted air-gap flux density. Moreover, the torque calculation error gradual increases with rise of current. In [20], the flux-linkage map of IPMSM is identified by experimental tests in motoring action. However, although this method can consider the magnetic saturation and spatial harmonics, it has a very complicated and time-consuming procedure that involves several measurements.

For accurate modelling, the iron losses must be included as they affect output torque. In [21,22], the iron loss analysis was derived based on FEA. In [23], the numerical calculation of iron loss' resistances based on FEA are presented. However, the modelling of iron loss would be very time-consuming using FEA. Hence, analytical methods are used. In [24], the calculation of iron loss of PMSM's stator considering DC-biased magnetic induction is introduced. Moreover, in [25,26], the iron losses are expressed in the form of d- and q-axes flux linkages or currents. However, the derivation of iron loss' coefficients still remained unsolved. Moreover, the effect of iron loss on electromagnetic behavior of IPMSMs have to be considered and analyzed.

This paper develops a high-fidelity and accuracy model for PMSMs. The proposed model fits all types of PMSMs. It represents accurately the performance of real machines by precise consideration of magnetic saturation, mutual coupling, spatial harmonics, and the iron loss effects. First, the FEA is employed to generate the magnetic characteristics of the tested machine. Then, these characteristics are validated experimentally. The experimental measurements aim basically to have a precise and calibrated finite element (FE) model that represents a real machine. The experimental measurements are very simple, and they include the measurement of PM flux linkage and the calibration of the BH curve of the magnetic steel material. Once, the FE model is calibrated precisely, it is used to generate full data of the machine. Second, the FE data are processed and rearranged to produce a simple and computationally efficient MATLAB Simulink model. Third, the effect of iron losses is achieved analytically and integrated within the MATLAB Simulink model. This paper considers a fractional slot concentrated winding 12/10 IPMSM. The experimental verifications are included to prove model accuracy and flexibility.

2. Conventional Model of IPMSM

The dynamic model of IPMSM in a d-q rotor reference frame is as follows [27–29]:

$$v_d = R_s i_d + \frac{d\lambda_d}{dt} - \omega_e \lambda_q = R_s i_d + L_d \frac{di_d}{dt} - \omega_e L_q i_q \quad (1)$$

$$v_q = R_s i_q + \frac{d\lambda_q}{dt} + \omega_e \lambda_d = R_s i_q + L_q \frac{di_q}{dt} + \omega_e L_d i_d + \omega_e \lambda_{PM} \tag{2}$$

where v_d and v_q , i_d and i_q , λ_d and λ_q , and L_d and L_q are d - and q -axes components of voltage, current, flux-linkage, and inductance, respectively. λ_{PM} depicts the flux-linkage of permanent magnets. R_s is the stator resistance. ω_e is the electrical angular speed.

The electromagnetic torque (T_e) of IPMSM has two components, namely, the reluctance torque and the magnet torque, as described in Equation (3).

$$T_e = \frac{3}{2} p i_q (\lambda_d i_q - \lambda_q i_d) = \frac{3}{2} p i_q (\lambda_{PM} + (L_d - L_q) i_d) \tag{3}$$

where p is the pole pairs.

The mechanical equation is described by Equation (4).

$$\frac{d\omega_m}{dt} = \frac{1}{J} (T_e - T_L - B\omega_m) \tag{4}$$

where J is the inertia, ω_m is the angular speed, B is the frictional coefficient, and T_L is the load torque.

Figure 1 shows the implementation of the conventional machine model (CMM) using Equations (1)–(4). The CMM uses a constant machine parameter. Hence, it neglects the magnetic saturation, mutual coupling, spatial harmonics, and iron loss effect. The CMM considers only the fundamental components and neglects harmonic fields that are the result of magnetic saturation, slotting, and variation of permeance with rotor position. The inaccurate model affects performance analysis and accurate prediction of drive system performance. Moreover, it compromises control quality in maximum torque per ampere (MTPA) and field weakening (FW) operations. Hence, an accurate model that includes magnetic saturation, mutual coupling, spatial harmonics, and iron loss effects is necessary.

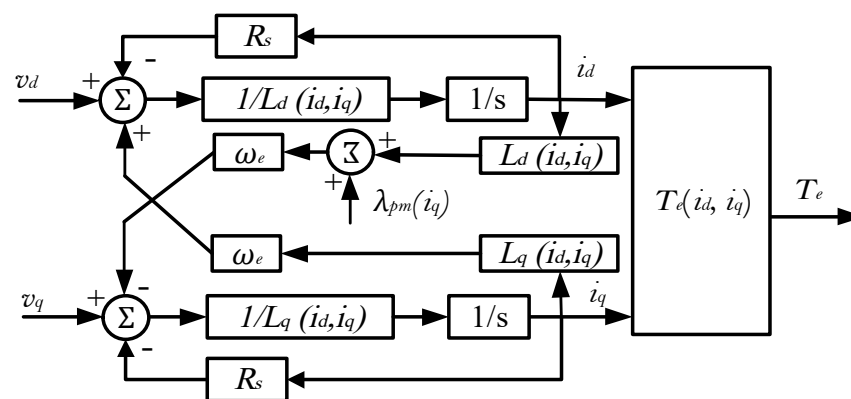


Figure 1. The schematic of the conventional machine model.

To consider only the magnetic saturation, the d - and q -axes inductances (L_d , L_q) are presented as functions of i_d and i_q . The obtaining of such relationships is not an easy task; several measurements must be conducted, which complicate the idea of obtaining a high-accuracy model for an IPMSM [30].

3. The Proposed Machine Model

For real IPMSMs, the fluxes (λ_d and λ_q) and the electromagnetic torque (T_e) are functions of currents (i_d and i_q) and rotor position (θ_i). These relationships can be written as given by Equation (5). Such an equation considers the saturation and spatial harmonics. Moreover, the torque components as well as the cogging torque are also considered.

The proposed machine model is developed as shown in Figure 2 considering the given fact of Equation (5). The inputs are the voltages v_d , and v_q . The flux-linkages (λ_d and λ_q) are estimated using Equation (6). The i_{da} and i_{qa} currents are obtained from the flux

inverse model that is given by Equation (7). The motor torque is obtained as a function of currents (i_{da} , i_{qa}) and rotor position θ_i . The iron losses are represented by the currents i_{d-fe} and i_{q-fe} . The estimation of iron losses within the model is given in a later section. Finally, the equation of mechanical motion is used to estimate the rotor position and speed.

$$\lambda_d = f(i_d, i_q, \theta_i); \quad \lambda_q = g(i_d, i_q, \theta_i); \quad T_e = T(i_d, i_q, \theta_i) \tag{5}$$

$$\lambda_d = \int (V_d - R_s i_d + \omega \lambda_q) dt; \quad \lambda_q = \int (V_q - R_s i_q - \omega \lambda_d) dt \tag{6}$$

$$i_d = f^{-1}(\lambda_d, \lambda_q, \theta_i); \quad i_q = g^{-1}(\lambda_d, \lambda_q, \theta_i) \tag{7}$$

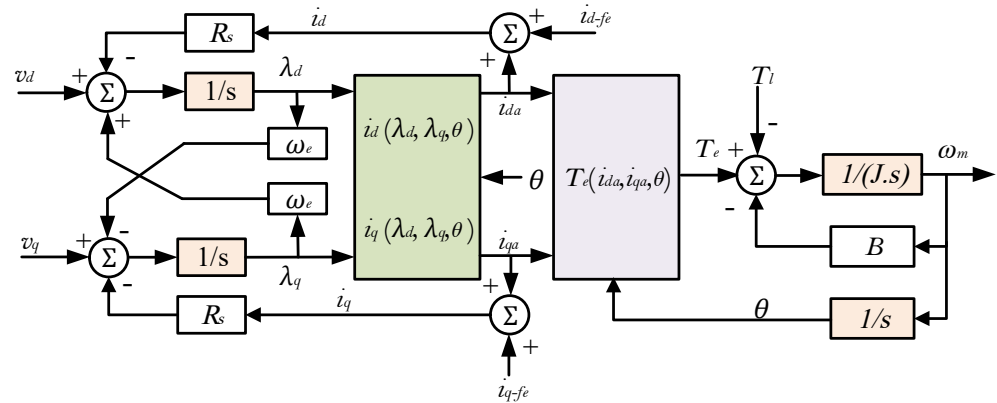


Figure 2. The schematic of the proposed IPMSM machine model.

The degree of modeling accuracy depends on calculation accuracy of magnetic characteristics ($\lambda_d(i_d, i_q, \theta_i)$, $\lambda_q(i_d, i_q, \theta_i)$, and $T_e(i_d, i_q, \theta_i)$) for the tested machine. As the IPMSM possess high nonlinear magnetic characteristics, the estimation of $\lambda_d(i_d, i_q, \theta_i)$, $\lambda_q(i_d, i_q, \theta_i)$, and $T_e(i_d, i_q, \theta_i)$ is not straightforward. Therefore, the FEA is employed to estimate the magnetic characteristics for the tested 12/10 IPMSM prototype.

Figure 3 shows the machine structure. It is a 12 slot, 10 magnet pole, 3 phase IPMSM. The rotor magnets are the V-shaped type. The stator has double layer windings for better torque ripple reduction. The nominal parameters and dimensions of IPMSM are shown in Table 1.

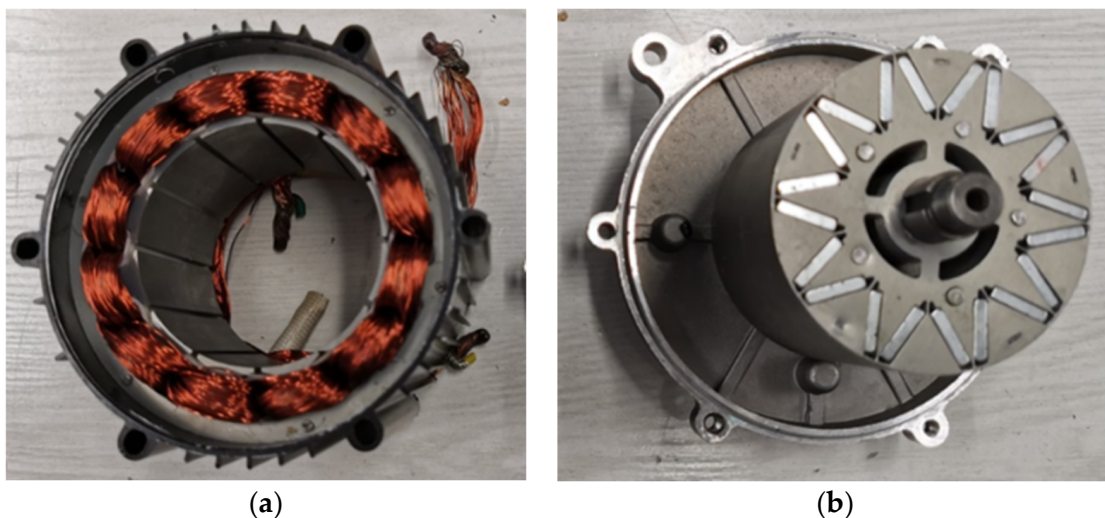


Figure 3. The IPMSM prototype: (a) stator, (b) rotor.

Table 1. The major parameters and dimensions of IPMSM.

Parameter	Value	Parameter	Value
No. of magnet poles	10	Stator outer diameter	120 mm
Number of slots	12	Height of stator pole	16 mm
Power	1200 W	Air-gap length	0.5 mm
Base speed	1000 r/min	Slot opening	2 mm
Rated torque	6.6 Nm	Magnet dimensions	14 × 7 mm
Shaft diameter	14 mm	Magnet material	N40SH
Rotor outer diameter	74 mm	Magnetic steel material	35WW270

3.1. Finite Element Analysis (FEA) of IPMSM

Despite the high accuracy of FEA compared to analytical methods, it needs the exact material properties and geometrical dimensions of the tested machine [31]. The main obstacle appears with the material properties, especially the PMs and magnetic steel properties (BH curve). If the material properties are given precisely, the FEA can provide very high accuracy of magnetic characteristics.

To ensure the inputted data to the FEA model represent accurately the real machine, this paper introduces a calibration method for the FEA model. The calibration is achieved based on the experimental measurements for the tested 12/10 IPMSM prototype. The experimental calibration is very important, as it can consider the manufacturing effects on both magnets and magnetic steel materials. It also can include the manufacturing tolerances and the physical changes that are included due to the manufacturing process.

3.1.1. Calibration of FEA Model

The aims of calibration is to obtain the real material properties for the tested IPMSM. These material properties will be inputted to the FEA model. Any error in material properties will lead to a calculation error in the magnetic characteristics of IPMSM. Therefore, the calculation accuracy of the FEA model depends basically on the accuracy of its inputted data.

The properties of permanent magnets (PMs) rarely coincide with the available data in manufacturers' datasheets. This is basically due to the manufacturing quality and tolerances, especially for low-cost motors. Probably, it will be decreased slightly less than the manufacturer datasheets [32]. Hence, the actual PM flux linkage must be measured experimentally to represent the real machine precisely.

The PM flux linkage (λ_{PM}) can be measured experimentally when the machine is working as a generator under no load. The no-load back EMF voltages are measured and recorded, preferably at high speeds. The higher speed is preferred to have a higher voltage on stator windings. The measurement errors in the case of a higher voltage range are lower compared to the case of lower voltage. Hence, high speed is preferred to reduce the measurement error in phase voltages and hence to estimate accurately the flux linkage of permanent magnets. λ_{PM} can be estimated using Equation (8). Due to the concentrated windings configuration, the fundamental component of phase voltage must be considered. Hence, Fast Fourier Transform (FFT) is conducted for the phase voltage, as seen in Figure 4.

First, the machine is operated as a generator with the help of a dc motor at a speed of 1708 r/min. The high speed (greater than rated) helps to reduce voltage error and hence to improve the measurement accuracy. The window of FFT is chosen as 5 cycles to ensure accurate analysis, as seen in Figure 4. The analysis is conducted for three phases (A, B, and C) to extract the average value of measured λ_{PM} that represents the real machine properly. The differences appear to be very small and can be ignored, as illustrated in Table 2.

$$\lambda_{PM} = \frac{V_{ph_peak} (Fundamental)}{2 * \pi * f} \quad (8)$$

where f is the frequency of back EMF voltage.

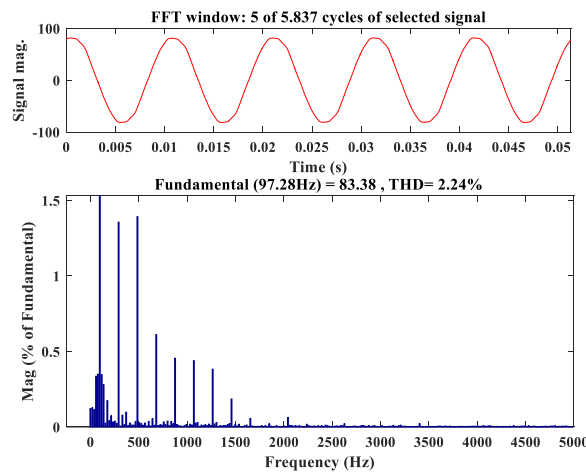


Figure 4. FFT of phase voltage at a speed of 1708 r/min.

Table 2. The measured flux linkage of PMs (λ_{PM}).

Phase	A	B	C
Measured λ_{PM} (in mWb)	136.41	135.00	136.45

The measured average PM flux linkage (λ_{PM}) is 135.95 mWb. The FEA model is then calibrated to produce the same flux linkage ($\lambda_{PM} = 135.95$ mWb). Hence, based on this measured value of λ_{PM} , the coercivity of PM in the FEA model is set to 848,000 A/m instead of 969,969 A/m from the manufacturers’ datasheets. The reduction ratio is 12.23%.

Lately, due to the huge interest of EVs, several magnetic steel materials have been introduced. These materials have gone through several tests, including the measurement of their BH curves. The tested motor is made from 35WW270 magnetic steel material. Its measured BH curve is available online. This curve fits accurately with the real machine. Hence, no calibration is needed for the BH curve of magnetic steel.

In case the BH curve data are not available in an accurate enough manner, the machine is operated as a motor with known currents i_d and i_q . Then, the developed motor torque is measured and recorded. After that, the measured torque is compared to the estimated torque from FEA under the same current values (i_d and i_q). The difference, if it exists, is adjusted by the BH curve of magnetic steel.

For now, the accurate coercivity of PM material is obtained. Moreover, the measured BH curve is also available online. Now the FEA model is ready to provide the precise magnetic characteristics for the tested machine.

A 2D FE model for the tested IPMSM is illustrated in Figure 5. The motor dimensions are given in Table 1. The model is built in finite element method magnetics (FEMM). The end effects of coils can be ignored due to the considerable axial length of the machine; hence, 3D analysis, which is very time consuming, is not necessary [33]. For the 2D FE model, the recent programs for FEA make the calculation much easier and speed up computations by static magnetic field analysis. The following assumptions are made: a zero magnetic vector potential for the outer surface of the stator; a constant air-gap length; isotropic rotor and stator materials; concentric stator and rotor poles; neglected core losses, MMF space harmonics, end-winding, and skin effects; and z-directed current density and magnetic vector potentials. Special attention is directed to the air-gap flux calculation, and a smaller mesh size is used for it. The FEA has 24,838 nodes and 49,292 elements.

3.1.2. Results of FEA

Figure 5 shows the distribution of flux density as well as the flux lines that are estimated from the FEA model. As noted, the highest flux densities are seen in rotor ribs and stator pole shoes. These parts are in deep saturation.

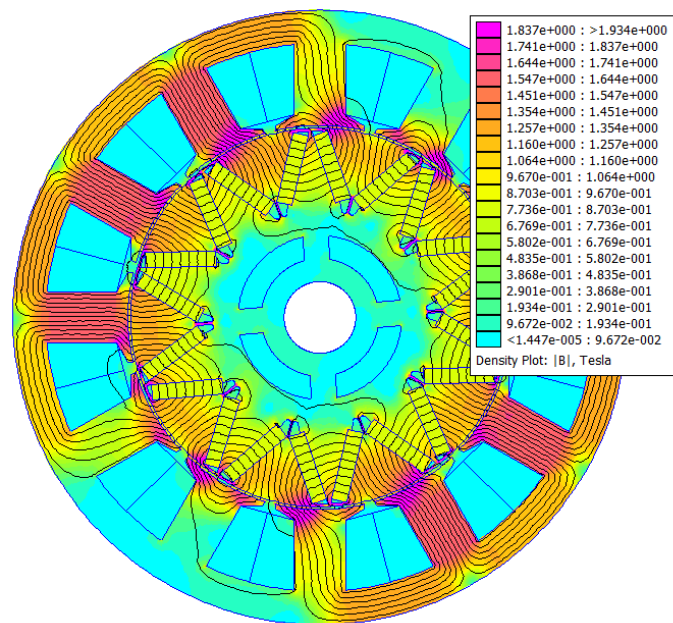


Figure 5. The flux lines and flux density at $i_q = 10$ A, $i_d = -3$ A, and $\theta_i = 0^\circ$.

The results of FEA are obtained as functions of currents i_d and i_q as well as θ_i . The currents i_d and i_q are changed from -25 to 0 A (26 points) and from 0 to 25 A (26 points), respectively. The current step is 1A. θ_i is changed from 0° to 72° insteps of 1 mech $^\circ$ (73 points). Therefore, it requires $(26 * 26 * 73 = 49,348)$ solutions to generate the full magnetic characteristics for the tested machine motor. The symmetry of the magnetic machine structure helps greatly to reduce the time and/or number of solutions either by plotting part of the machine or by choosing part of the rotor rotation.

The inductances L_d and L_q are calculated using Equations (9) and (10), respectively.

$$L_d = \frac{\lambda_d - \lambda_{PM}}{i_d} \quad \text{at } i_q = \text{constant} \tag{9}$$

$$L_q = \frac{\lambda_q}{i_q} \quad \text{at } i_d = \text{constant} \tag{10}$$

Figure 6 shows the flux-linkages ($\lambda_d(i_d, i_q, \theta_i)$, $\lambda_q(i_d, i_q, \theta_i)$), torque $T_e(i_d, i_q, \theta_i)$, and inductances ($L_d(i_d, i_q, \theta_i)$, $L_q(i_d, i_q, \theta_i)$) as functions of i_d , i_q at $\theta_i = 0$. As seen, the flux linkages, torque, and inductances show highly nonlinear relations with currents. As seen in Figure 6, the d - and q -axes inductances (L_d , L_q) decrease with the increase of q -axis current i_q over the full range of d -axis current i_d .

3.2. Production of MATLAB Simulink Model

The proposed machine model that is given in Figure 2 consists of three main parts: first, the torque estimation $T_e(i_d, i_q, \theta_i)$, which is a straightforward task, as the obtained data from FEA can be stored in the form of a 3D LUT; second, the representation of iron losses by the currents i_{d-fe} and i_{q-fe} , which is included in a later section; and third, the estimation of currents $i_d(\lambda_d, \lambda_q, \theta_i)$ and $i_q(\lambda_d, \lambda_q, \theta_i)$. As noted, this is an inverse solution for the obtained data from FEA. The FEA gives the fluxes as functions of currents and positions. The required the characteristics $i_d(\lambda_d, \lambda_q, \theta_i)$ and $i_q(\lambda_d, \lambda_q, \theta_i)$ to be in the inverse form; the currents are functions of fluxes and positions.

3.2.1. Inverse Solution of Currents versus Flux Linkages

Equation (11) is used to represent the error between required fluxes (λ_{do} and λ_{qo}) and actual fluxes, $\lambda_d(i_d, i_q, \theta_i)$ and $\lambda_q(i_d, i_q, \theta_i)$, that correspond to currents i_d and i_q . The currents i_d and i_q are obtained by minimizing the objective function F_{obj} using an iterative

process in which λ_d and λ_q are interpolated on FEA-calculated flux maps. Figure 7 shows the flowchart of this process. First, the desired or commanded fluxes (λ_{do} and λ_{qo}) are inputted. Then, the currents (i_d and i_q) are changed with small steps ($\Delta i_d = 0.1$ A and $\Delta i_q = 0.1$ A). for each value of currents (i_d and i_q) within the iterative process, the fluxes are estimated from the flux maps of Figure 6. Finally, the objective function is estimated for obtained current and flux vectors, and then the currents (i_d and i_q) that corresponds to minimum flux error (minimum F_{obj}) are output as the optimal solution of currents. Figure 8 shows the obtained optimal i_d and i_q currents after the Inverse solution of currents versus flux linkages.

$$F_{obj}(i_d, i_q) = \min\{|\lambda_d(i_d, i_q, \theta_i) - \lambda_{do}| + |\lambda_q(i_d, i_q, \theta_i) - \lambda_{qo}|\} \tag{11}$$

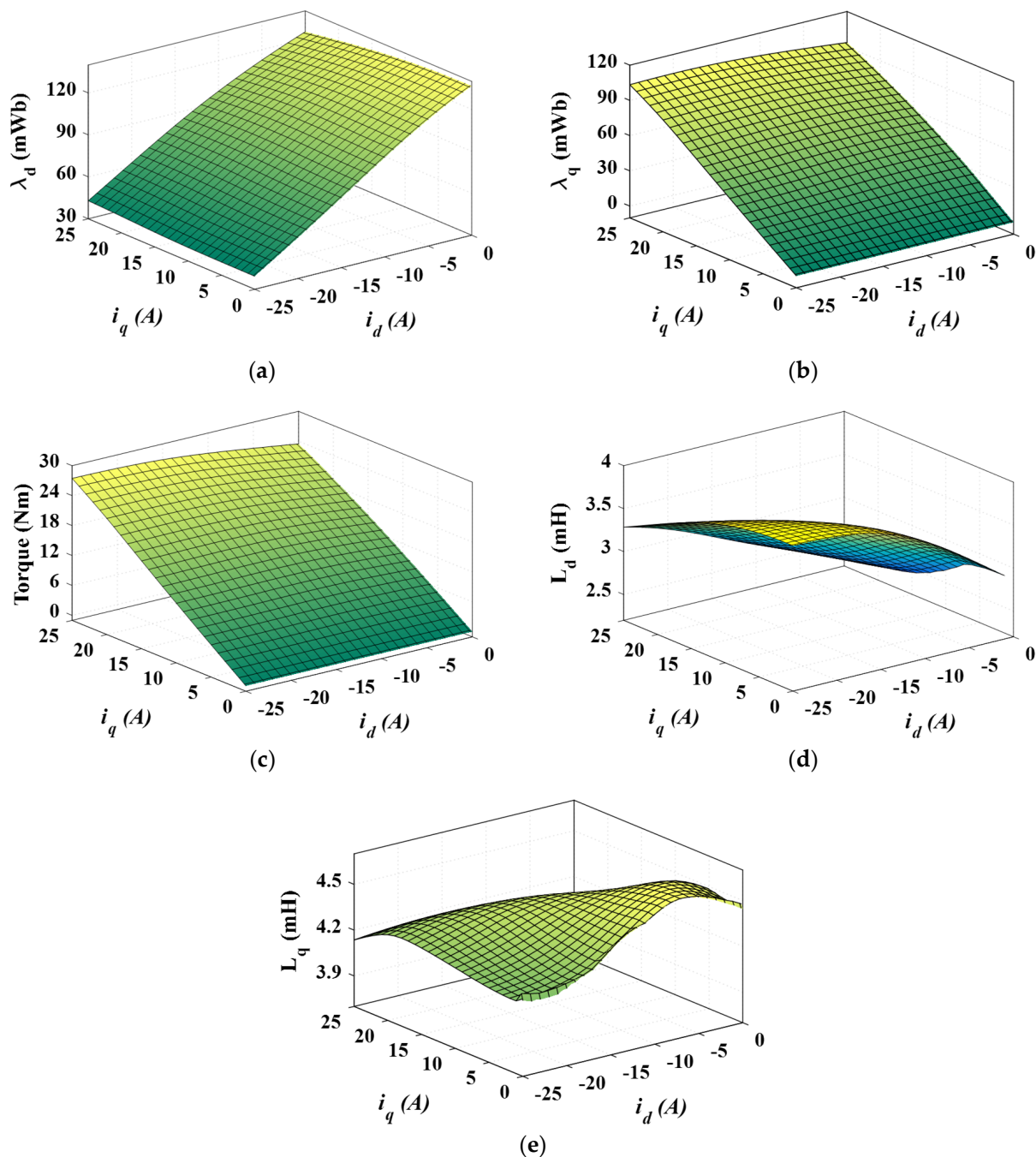


Figure 6. The FEA-calculated (a) λ_d , (b) λ_q , (c) torque, (d) L_d , and (e) L_q .

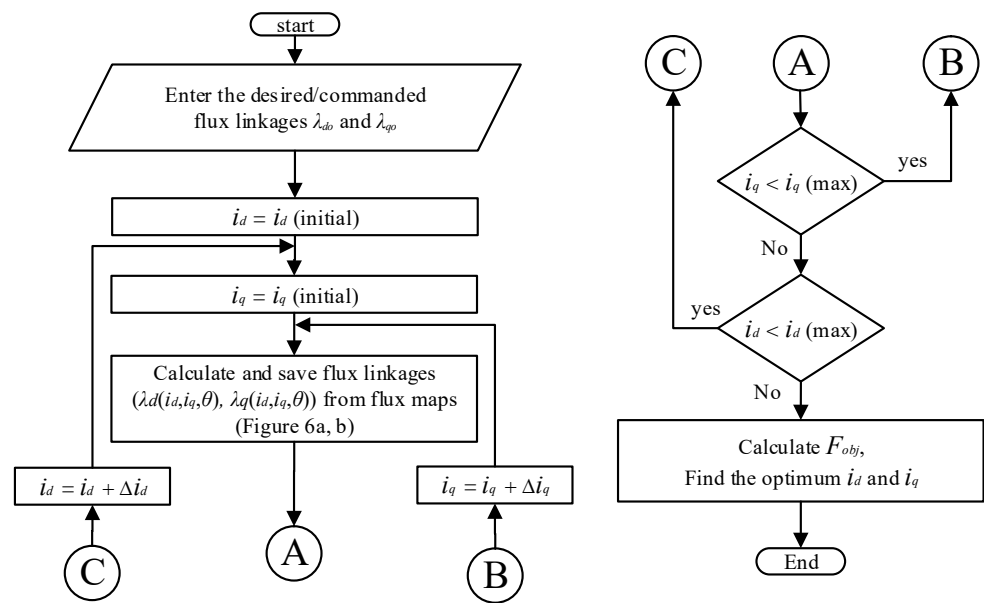


Figure 7. Flowchart for the inverse solution of currents versus flux linkages.

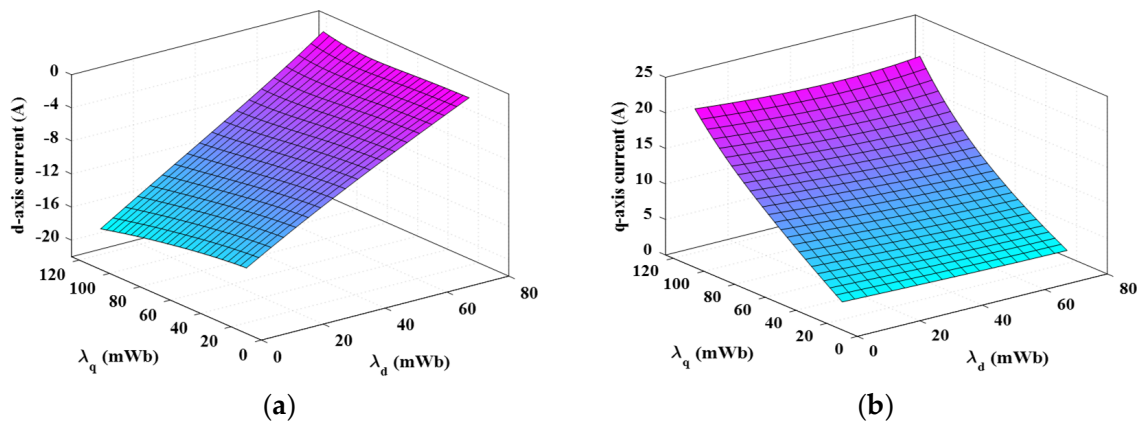


Figure 8. The current maps: (a) d-axis current, (b) q-axis current.

The obtained i_d and i_q currents of Figure 8 are inputted to flux maps (Figure 6a,b). The resultant fluxes are compared to their corresponding flux values. The flux errors are shown in Figure 9. As noted, the maximum error is very small and can be ignored. The small error reflects the accuracy of the inverse solution and hence the accuracy of the proposed model.

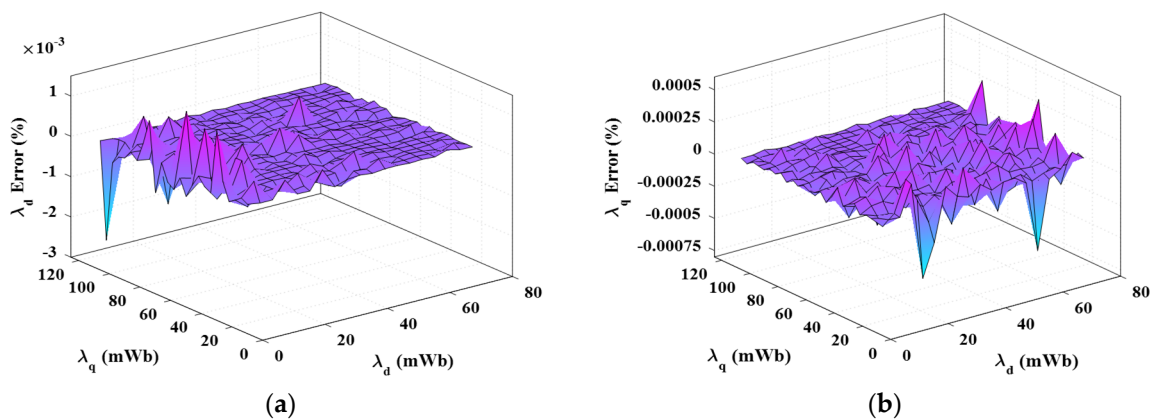


Figure 9. The flux error maps: (a) d-axis flux error, (b) q-axis flux error.

3.2.2. Estimation of Iron Losses

The iron losses per unit volume can be estimated by the well-known Bertotti formula, as a function of frequency (f) and maximum flux density (B_m), as given by Equation (12) [34,35]. k_h , k_c , and k_e are the coefficients of hysteresis, eddy current, and additional losses, respectively. k_c is calculated as a function of material conductivity (σ) and lamination thickness (k_d), as given by Equation (13).

Equation (14) is a reformulation of Equation (12). The flux densities are converted to their corresponding flux-linkages based on machine dimensions and winding information. The equivalent iron loss resistance (R_c) is given by Equation (16).

$$dP_{fe} = k_h f B_m^\alpha + k_c f^2 B_m^2 + k_e f^{1.5} B_m^{1.5} \tag{12}$$

$$k_c = \pi^2 \sigma k_d^2 / 6 \tag{13}$$

$$P_{fe} = k_1 (\lambda_d^2 + \lambda_q^2) + k_2 (\lambda_d^{1.5} + \lambda_q^{1.5}) \tag{14}$$

$$k_1 = (k_h f + k_c f^2) (V_t / A_{tc}^2 + V_y / A_{yc}^2); \tag{15}$$

$$k_2 = k_e f^{1.5} (V_t / A_{tc}^{1.5} + V_y / A_{yc}^{1.5})$$

$$R_c = \omega_e^2 / k_1 \tag{16}$$

where V_t and V_y , h_t and h_y , and A_t and A_y are the volumes, heights, and areas for the stator tooth and yoke, respectively.

The equivalent circuit of an IPMSM representing iron losses P_{fe} and copper losses P_{cu} is demonstrated in the rotor reference frame as shown in Figure 10. The iron and copper losses are represented by the resistances R_c and R_s , respectively. i_{da} and i_{qa} are the magnetizing currents. They can be calculated using Equation (17). The torque expression in terms of i_{da} and i_{qa} is given by Equation (18).

$$i_{da} = i_d - i_{d-fe} = i_d - \frac{(v_d - R_s i_d)}{R_c} \tag{17}$$

$$i_{qa} = i_q - i_{q-fe} = i_q - \frac{(v_q - R_s i_q)}{R_c}$$

$$T_e = \frac{3}{2} p i_{qa} (\lambda_{PM} + (L_d - L_q) i_{da}) \tag{18}$$

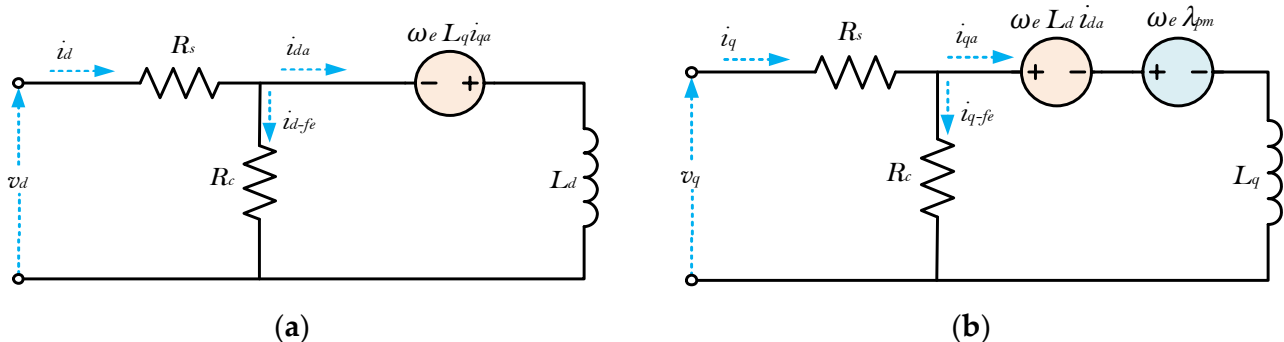


Figure 10. The d- and q-axes equivalent circuits of an IPMSM with iron losses: (a) d-axis, (b) q-axis.

4. Model Verification

The proposed model, shown in Figure 2, was implemented in the MATLAB/Simulink environment. It is validated in two ways. The first was a comparison with the FEA model, and the second was by the experimental measurements on a physical 12/10 IPMSM prototype. Moreover, the experimental verifications were achieved in both the generator and motor actions.

4.1. Compared to FEA Model

To check the accuracy of proposed model, first, the Simulink model was run at a specific operating point based on the field-oriented control (FOC) algorithm, and the resulting current (i_d, i_q) waveforms were extracted. These currents (i_d, i_q) were then injected into the FEA model to estimate the fluxes and electromagnetic torque.

The comparison was achieved at speed of 1500 r/min and stator current of 10 A. The waveforms of current (i_d, i_q) are as shown in Figure 11a,b. The d- and q-axes flux linkages were estimated by the FEA model and then compared to corresponding values calculated within the MATLAB Simulink model. The comparison is given in Figure 11c,d. It was observed that the FEA-predicted d- and q-axes fluxes as well as the torque, as seen in Figure 11e, and could be completely reproduced by the MATLAB Simulink model. Note that the Simulink model required a very short time compared to FEA to produce the same results.

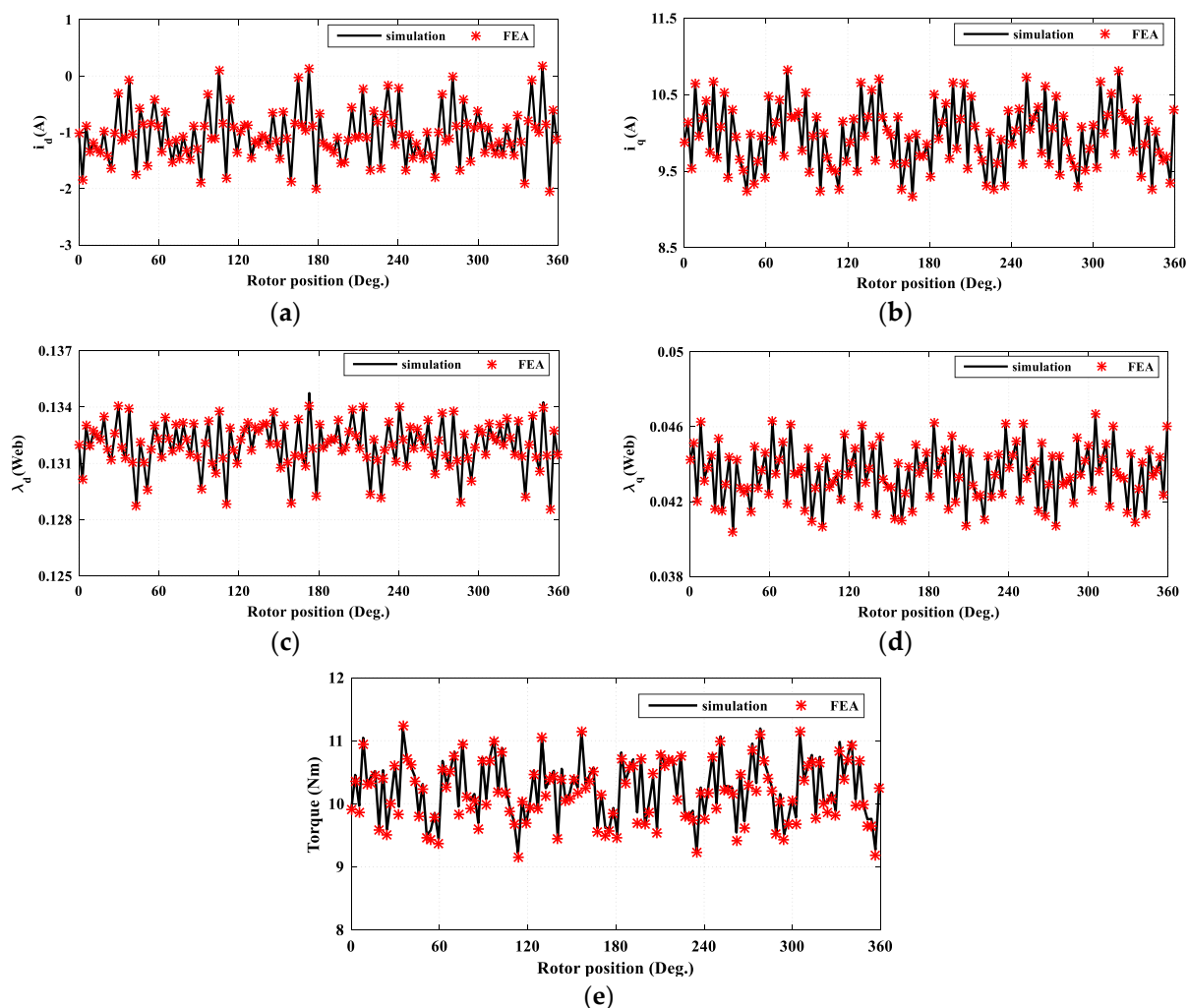


Figure 11. Comparisons of Simulink and FEA: (a) d-axis current; (b) q-axis current; (c) d-axis flux; (d) q-axis flux; (e) torque.

4.2. Experimental Verification as a Generator

To verify the effectiveness of the proposed Simulink model, an experimental platform was set up, as shown in Figure 12. The drive system included a three phase inverter, an IGBT gate-driver, current transducers (LEM LA100-P), voltage transducers (LEM LV 25-P), a torque sensor (Lorenz DR 2112), an incremental encoder (1024 PPR), a data acquisition board (NI 6229 DAQ), an electromagnetic brake, and a digital signal processor (C6713 DSP).

The DSP was connected to an FPGA for better timing. The data were collected online with the help of a daughter card using MATLAB.

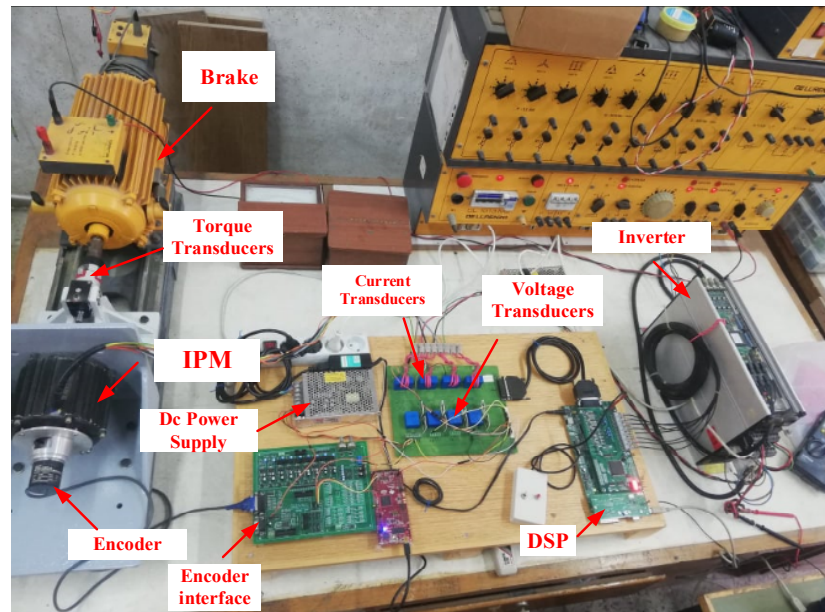


Figure 12. The practical implementation of the measurement platform.

The IPMSM was operated as a generator. It was driven by a dc motor. First, Figure 13 shows the experimental results under no load at 1708 r/min. The experimental results showed three phases' currents, the three phases' voltages, and electromagnetic torque. The average value of no-load torque, as seen in Figure 13c, was 0.39 Nm, which basically represents iron and friction losses. The torque ripple was very noticeable. Figure 13d shows a comparison between the measured phase voltage and the phase voltage obtained from FEA. As observed, a perfect match is seen in Figure 13d that reflects the accuracy of the FEA model and hence the accuracy of the proposed model.

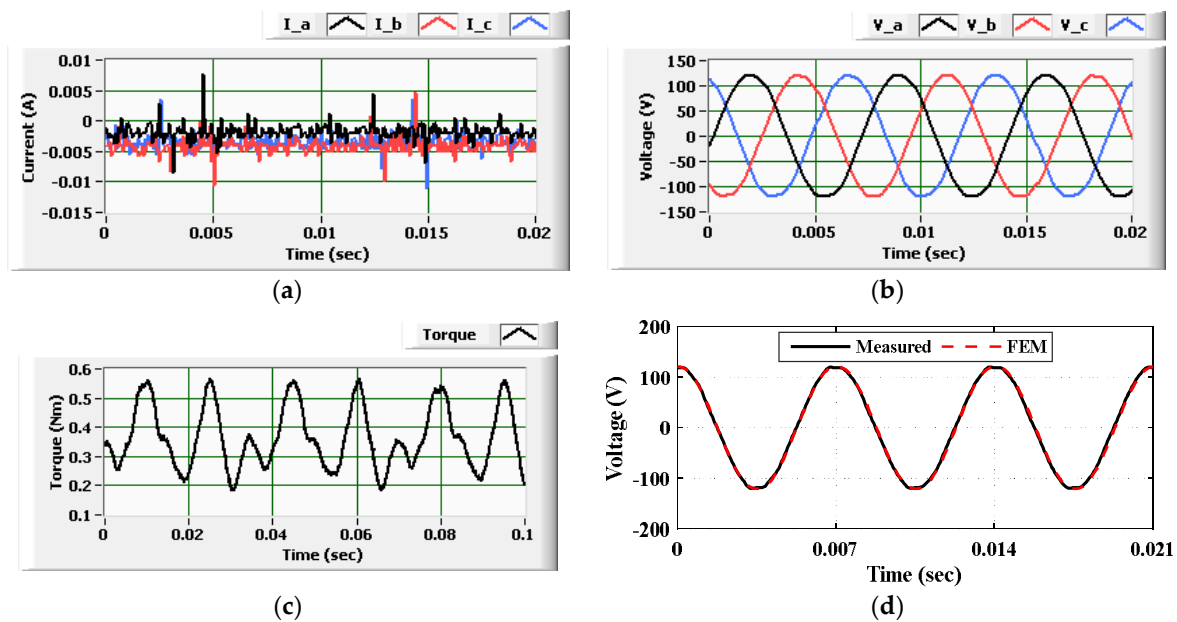


Figure 13. The experimental results at no-load as a generator. (a) The waveform of phases' currents; (b) the waveform of phases' voltages; (c) the electromagnetic torque; (d) the measured and FE-predicted phase voltage.

Second, Figure 14a–c show the experimental results under loading conditions as a generator. The IMPSM was driven at a speed of 854 r/min, and the terminals were connected to a resistive load. Figure 14d shows a comparison between the measured phase voltage and the phase voltage obtained from FEA. As observed, a perfect match was also seen.

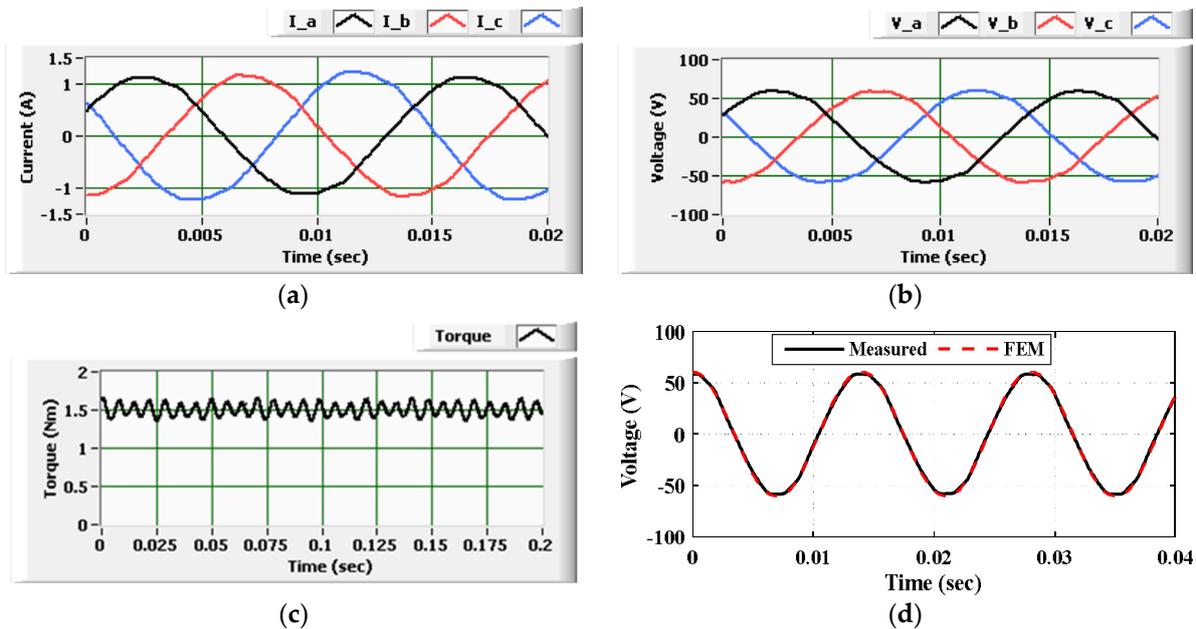


Figure 14. The experimental results under loading as a generator. (a) The waveform of phases' currents; (b) the waveform of phases' voltages; (c) the electromagnetic torque; (d) the measured and FE-predicted phase voltage.

Figure 15a shows a comparison between the measured torque (by a torque sensor) and the predicted FEA torque under loading conditions of Figure 14. As seen, the torque sensor was not fast enough to capture all the torque details. The full torque details, including torque ripple, was well displayed by the FEA model. Moreover, Figure 15b gives the average torque values. The difference between the measured and FEA came from the fact that FEA does not consider iron loss effect. The FEA provides a magnetostatic solution. The iron loss effect was not considered in the FEA model as it is usually evaluated in post processes of most commercial FEA tools. On the other hand, the iron loss was included within the proposed model. Hence, very good agreement was observed between the measured torque signal and the simulated torque signal, as seen in Figure 15b.

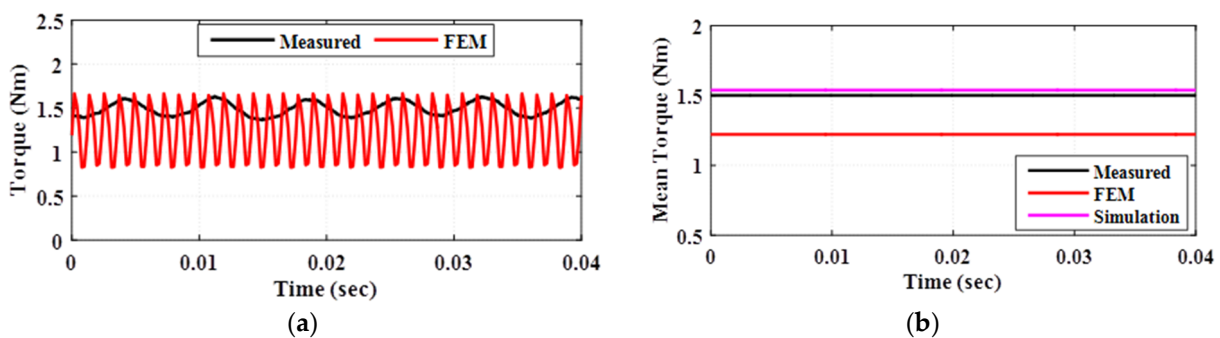


Figure 15. Comparison between measured and FE-predicted torque as a generator: (a) torque waveform; (b) average torque.

Table 3 shows the analysis details for torque data. As illustrated, the torque error for the FEA model was 18.8%. Hence, the FEA model was not accurate enough to represent the

real machine, as it neglects iron loss effect. On the contrary, the proposed Simulink model provided a torque error of 2.13%, which may have been a result of stray losses, variation of dc voltage, measurement errors (signal errors and quantization errors), tolerances in machine dimensions, and degradation of material properties. Hence, the proposed model succeeded in representing the real machine accurately.

Table 3. Summary of torque results.

	Measured	FEM	Simulation
Average Torque (Nm)	1.505	1.222	1.537
Torque Error (Nm)	-----	0.283	0.032
Torque Error (%)	-----	18.80	2.12

4.3. Experimental Verification as a Motor

Finally, experimental tests for the IPMSM in motoring action were achieved based on the FOC algorithm. The dc link voltage was set to 200 V. First, the FOC algorithm was tested to ensure proper tracking operation. Figure 1 shows the performance of the FOC algorithm under sudden changes of reference currents (i_{d-ref} and i_{q-ref}). As seen in Figure 16a,b, i_{q-ref} changed as a triangular wave at a frequency of 20 Hz. The motor speed was 486 r/min. As seen in Figure 16c,d, both i_{d-ref} and i_{q-ref} changed as square waves at a frequency of 10 Hz. The motor speed was 488 r/min. As noted, for both cases, the FOC algorithm worked efficiently, as the motor could track the reference d- and q-axes currents properly. Moreover, the three phases currents were symmetric and sinusoidal.

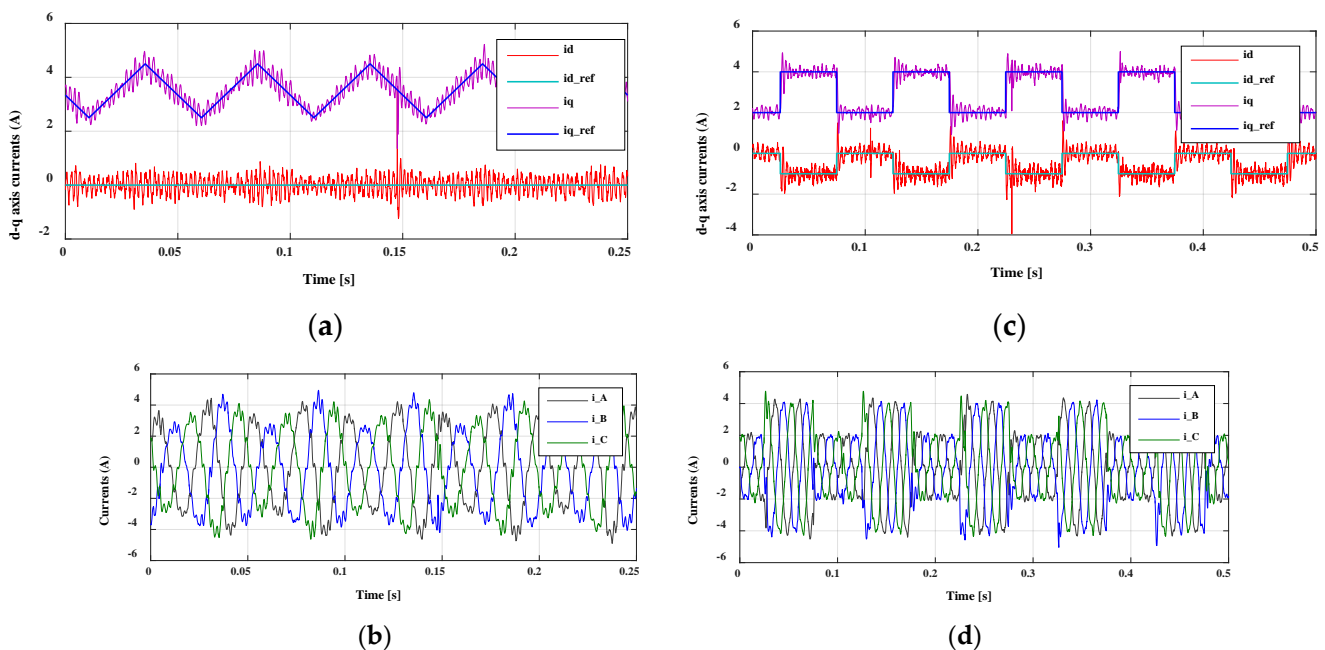


Figure 16. The measured waveforms: (a) the measured d- and q-axes currents with i_{q-ref} is changing as a triangular wave; (b) the measured three-phases' currents with i_{q-ref} is changing as a triangular wave. (c) the measured d- and q-axes currents with i_{d-ref} and i_{q-ref} changing as square waves; (d) the measured three-phases' currents with i_{d-ref} and i_{q-ref} changing as square waves.

Second, the motor was operated under a steady state condition with reference currents $i_{d-ref} = 0$ and $i_{q-ref} = 3.5$ A. The loading torque was adjusted to reach a speed of 555 r/min. The measured waveforms were recorded, as seen in Figure 17a–c. Then, the same case was simulated within the MATLAB Simulink model. The simulation results are given in Figure 17d–f. As noticed, very good agreement was observed between measurement and simulation.

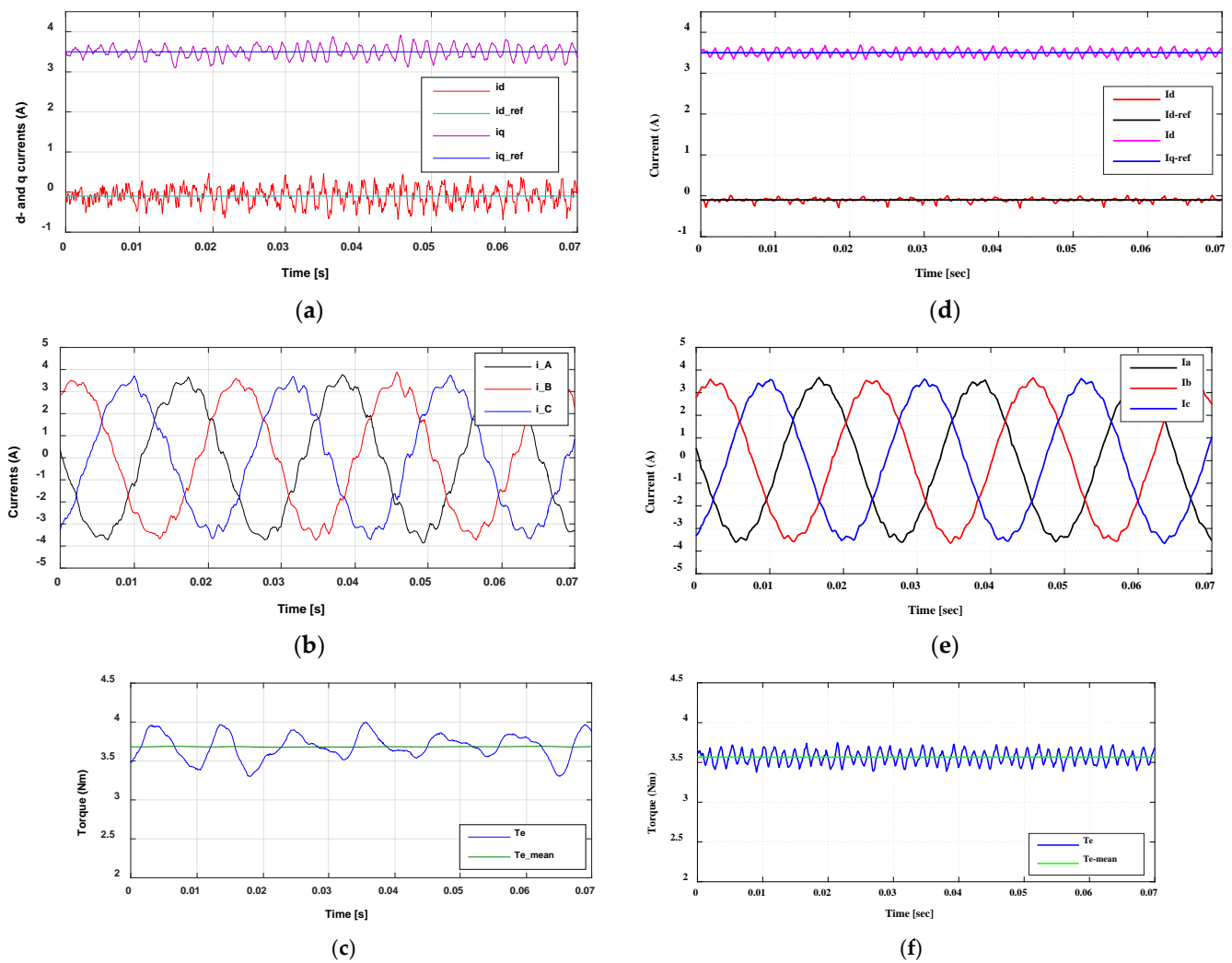


Figure 17. Comparison between measurement and simulation results as a motor: (a) the measured direct and quadrature currents; (b) the measured waveform of phases' currents; (c) the measured electromagnetic torque; (d) the simulated direct and quadrature currents; (e) the simulated waveform of phases' currents; (f) the simulated electromagnetic torque.

Table 4 gives the torque analysis data. It compares the measured and the simulated torques. The torque error was 3.26% which may be a result of measurement errors. Moreover, the mechanical coupling between the IPMSM and loading magnetic brake could be a primary reason for torque error, as improper mechanical coupling could affect friction losses. As a result, the proposed model is accurate enough to represent real machine performance.

Table 4. The measured and simulated torque results.

	Measured	Simulation	Torque Error (Nm)	Torque Error (%)
Average Torque (Nm)	3.68	3.56	0.12	3.26

Recently, many researchers have become interested in MTPA and maximum efficiency per ampere (MEPA) control for IPMSM, as they are very important, especially for high power machines such as in EV applications. The basic idea for MTPA and MEPA is to define the current angle that corresponds to the desired criteria (maximum torque or maximum efficiency). The proposed model can easily be used for such purposes. The obtained current angles can be further employed in real implementations to achieved MTPA and MEPA.

Figure 18 shows a comparison of the measured and simulated torque versus current angle. The current angle was changed from 0° to 50° in steps of 5°. The maximum current

was set to 3 A. The motor was running in an open loop current control. The motor speed was adjusted by the loading dc brake. The test was done at 500 r/min. As noted, due to the reluctance torque of IPMSM, the maximum torque did not occur at a zero-current angle, such as in surface-mounted PMSM. As seen, the maximum torque occurred around a 5° current angle. Moreover, very good agreement was observed between measurement and simulation, as seen in Figure 18a. The maximum torque error over 11 points of comparison was 0.12 Nm at a current angle of 0° , as illustrated by Figure 18b. It corresponded to an error of 4.1%, as seen in Figure 18c. On the other hand, the average torque error over 11 points of comparison was 0.0449 Nm, which corresponded to a percentage of 1.7422%, which is a small error and could be a result of measurement errors, assumptions in the FEA model, variations of dc voltage, or effects of temperature on machine parameters such as magnets and resistance.

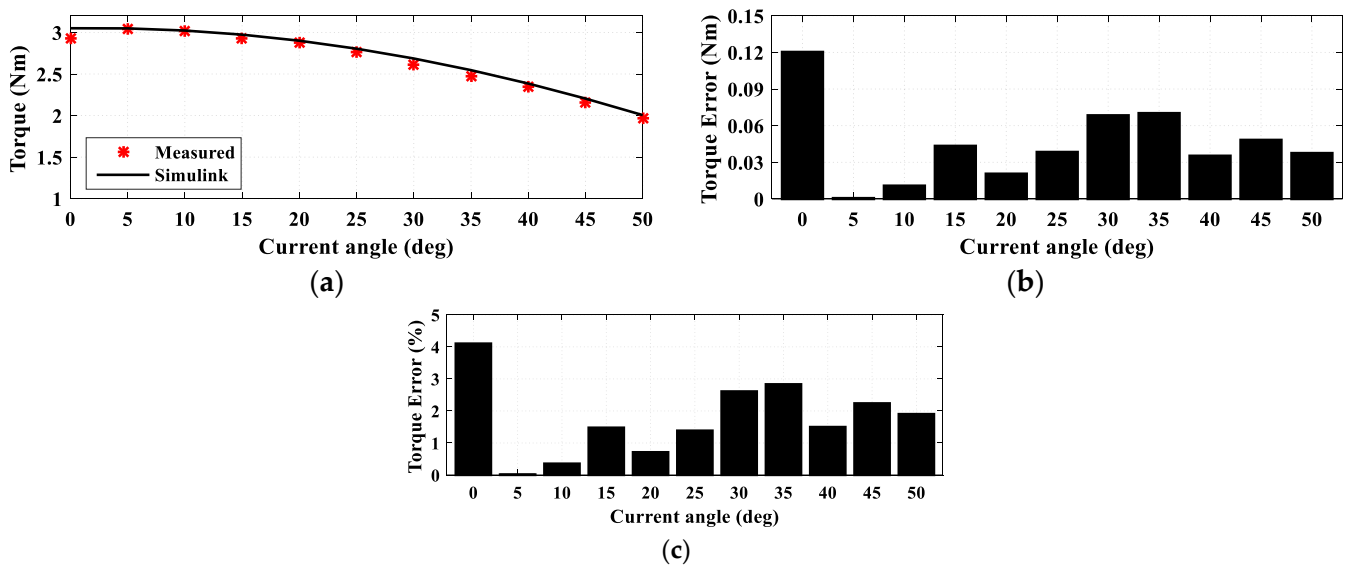


Figure 18. Comparison between the measured and simulated torque vs. current angle: (a) measured and simulated torques vs. current angle; (b) torque error in Nm; (c) percentage torque error.

The model accuracy will remain similar for wider speed ranges as long as the control algorithm (FOC) provides good tracking behavior. If the FOC fails tracking, this will not affect the model accuracy, which means that the control algorithm (FOC) itself needs improvements, not the proposed machine model.

5. Summary of Proposed Method

Figure 19 shows a flowchart that explains step by step the proposed modeling method. First, the machine dimensions, material properties, and configurations of current circuits are defined. Second, the FE model of the machine is constructed. The FE model must be precisely configured to represent real machine behavior. Any mismatches in input data to the FE model will lead to undesirable and huge errors. Hence, the experimental verification of the FE model is of great importance. Third, the FE model is validated by comparing the no-load and loading voltages of the machine as a generator. If the accuracy is accepted and hence the PM flux linkage is inputted precisely, then one can proceed to calculate the full magnetic characteristics of machine. on the contrary, if the accuracy is not satisfactory, then measurement of the PM flux linkage must be done precisely after an FFT of phase voltage, as described in Section 3.1.1. After that, the production of the full magnetic characteristics of the machine can be achieved. Fourth, the development of the MATLAB Simulink model is done using the FEA data after precise calibrations. The MATLAB Simulink model requires an inverse solution of currents versus flux linkages, as discussed in Section 3.2.1. It also involves the estimation of iron losses and its involvement within the

MATLAB Simulink model, as described in Section 3.2.2. The final step is to validate the MATLAB Simulink model experimental when the machine is operated as a motor.

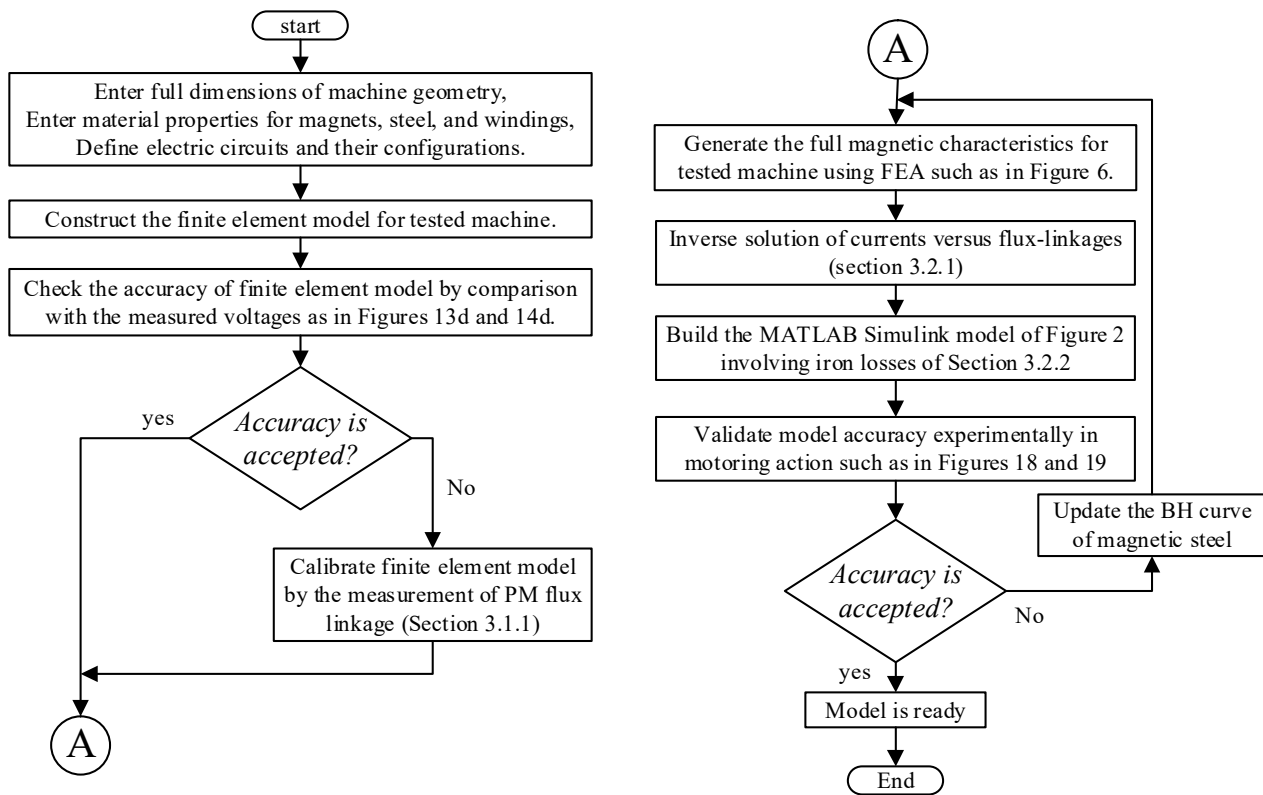


Figure 19. Flowchart of the proposed modeling method.

6. Conclusions

This paper develops an accurate modeling method for PMSMs. First, the proposed model exhibits high fidelity in predicting real machine behavior while providing a computationally efficient solution. It presents a powerful solution for detailed analysis of all kinds of PMSMs for further performance analysis or for developing accurate control algorithms. It also helps to analyze machine losses and estimate real machine efficiency. Accurate loss modeling and efficiency estimation are key interests for current and future research related to several industrial applications such as electric vehicles. Second, the proposed model considers accurately iron losses effects as well as the effects of magnetic saturation, spatial harmonics, and mutual coupling. Third, it not only guaranties the production of a high accuracy model but also involves the manufacturing effects by the calibration of the FEA model based on experimental measurements. As seen by the results, the good match between simulation and experimental measurements reflects the high model accuracy. The average percentage of torque error between measurement and simulation is 1.7422%, which is a small and acceptable error.

Author Contributions: Conceptualization, H.E.; Data curation, H.E.; Formal analysis, H.E. and M.K.A.; Funding acquisition, L.S.; Investigation, H.E. and M.K.A.; Methodology, H.E.; Resources, L.S.; Software, H.E.; Supervision, M.K.A. and M.A.E.; Validation, H.E.; Writing—original draft, H.E.; Writing—review and editing, H.E. and M.K.A. All authors have read and agreed to the published version of the manuscript.

Funding: This research received no external funding.

Conflicts of Interest: The authors declare no conflict of interest.

Nomenclature

Symbol	Definition	Unit
A_t, A_y	The areas of stator pole/tooth and yoke	m ²
B	The combined rotor and load viscous friction coefficient	kg·m ²
B_m	The peak value of magnetic flux density	Wb/m ²
f	The frequency of back EMF voltage	Hz
F_{obj}	The objective function	
h_t, h_y	The heights of stator pole/tooth and yoke	m
i_d, i_q	The d- and q-axes components of stator current	A
i_{da}, i_{qa}	The d- and q-axes components of magnetizing currents	A
i_{d-fe}, i_{q-fe}	The d- and q-axes components of currents that represents iron losses	A
i_{d-ref}, i_{q-ref}	The d- and q-axes components of reference current	A
J	The combined rotor and load inertia coefficient	kg·m ² ·s
k_c	The coefficients of eddy current losses	W/m ³
k_d	The lamination thickness	m
k_e	The coefficients of additional losses	W/m ³
k_h	The coefficients of hysteresis losses	W/m ³
L_d, L_q	The d- and q-axes components of inductance	H
p	The number of pole pairs	
P_{cu}	The copper losses	W
P_{fe}	The iron losses	W
R_c	The iron loss resistance	Ω
R_s	The phase resistance	Ω
T_e	The total electromagnetic torque	N·m
T_L	The load torque	N·m
v_d, v_q	The d- and q-axes components of phase voltage	V
V_t, V_y	The volumes of stator pole/tooth and yoke	m ³
V_{ph_peak}	The peak value of phase voltage	V
θ_i	The rotor position	Deg
λ_d, λ_q	The d- and q-axes components of flux-linkage	Wb
$\lambda_{do}, \lambda_{qo}$	The commanded d- and q-axes flux-linkages	Wb
λ_{PM}	The flux-linkage of permanent magnets	Wb
ω_e	The electrical angular speed	Rad/s
ω_m	The angular velocity of rotor	Rad/s
σ	material conductivity	S/m

References

- An, X.; Liu, G.; Chen, Q.; Zhao, W.; Song, X. Adjustable Model Predictive Control for IPMSM Drives Based on Online Stator Inductance Identification. *IEEE Trans. Ind. Electron.* **2021**, *69*, 3368–3381. [[CrossRef](#)]
- Kim, H.-S.; Sul, S.-K. Real-Time Torque Control of IPMSM Under Flux Variations. *IEEE J. Emerg. Sel. Top. Power Electron.* **2020**, *10*, 3345–3356. [[CrossRef](#)]
- Elsherbiny, H.; Ahmed, M.K.; Elwany, M. Comparative Evaluation for Torque Control Strategies of Interior Permanent Magnet Synchronous Motor for Electric Vehicles. *Period. Polytech. Electr. Eng. Comput. Sci.* **2021**, *65*, 244–261. [[CrossRef](#)]
- Ni, R.; Xu, D.; Wang, G.; Ding, L.; Zhang, G.; Qu, L. Maximum Efficiency Per Ampere Control of Permanent-Magnet Synchronous Machines. *IEEE Trans. Ind. Electron.* **2014**, *62*, 2135–2143. [[CrossRef](#)]
- Balamurali, A.; Feng, G.; Lai, C.; Tjong, J.; Kar, N.C. Maximum Efficiency Control of PMSM Drives Considering System Losses Using Gradient Descent Algorithm Based on DC Power Measurement. *IEEE Trans. Energy Convers.* **2018**, *33*, 2240–2249. [[CrossRef](#)]
- Huang, S.; Wu, G.; Rong, F.; Zhang, C.; Huang, S.; Wu, Q. Novel Predictive Stator Flux Control Techniques for PMSM Drives. *IEEE Trans. Power Electron.* **2018**, *34*, 8916–8929. [[CrossRef](#)]
- Li, G.; Hu, J.; Li, Y.; Zhu, J. An Improved Model Predictive Direct Torque Control Strategy for Reducing Harmonic Currents and Torque Ripples of Five-Phase Permanent Magnet Synchronous Motors. *IEEE Trans. Ind. Electron.* **2018**, *66*, 5820–5829. [[CrossRef](#)]
- Li, S.; Han, D.; Sarlioglu, B. Modeling of Interior Permanent Magnet Machine Considering Saturation, Cross Coupling, Spatial Harmonics, and Temperature Effects. *IEEE Trans. Transp. Electrification.* **2017**, *3*, 682–693. [[CrossRef](#)]
- Liang, W.; Wang, J.; Lu, T.; Fang, W. A New Method for Multiple Finite-Element Models in Cosimulation with Electrical Circuit Using Machine Multiloop Modeling Scheme. *IEEE Trans. Ind. Electron.* **2014**, *61*, 6583–6590. [[CrossRef](#)]
- Parasiliti, F.; Villani, M.; Tassi, A. Dynamic analysis of synchronous reluctance motor drives based on Simulink® and finite element model. In Proceedings of the IECON Proceedings (Industrial Electronics Conference), Paris, France, 7–10 November 2006; pp. 1516–1520. [[CrossRef](#)]

11. di Leonardo, L.; Parasiliti, F.; Tursini, M.; Villani, M. Transient analysis of PM synchronous motor drives by finite element model co-simulation. In Proceedings of the IECON Proceedings (Industrial Electronics Conference), Vienna, Austria, 10–13 November 2013; pp. 6834–6840. [[CrossRef](#)]
12. Kano, Y.; Watanabe, K.; Kosaka, T.; Matsui, N. A Novel Approach for Circuit-Field-Coupled Time-Stepping Electromagnetic Analysis of Saturated Interior PM Motors. *IEEE Trans. Ind. Appl.* **2009**, *45*, 1325–1333. [[CrossRef](#)]
13. Queval, L.; Ohsaki, H. Nonlinear abc-Model for Electrical Machines Using N-D Lookup Tables. *IEEE Trans. Energy Convers.* **2014**, *30*, 316–322. [[CrossRef](#)]
14. Bose, B.K. Neural Network Applications in Power Electronics and Motor Drives—An Introduction and Perspective. *IEEE Trans. Ind. Electron.* **2007**, *54*, 14–33. [[CrossRef](#)]
15. Zhang, K.; Sun, T.; Xie, G.; Zhang, J.; Xiong, G.; Liang, J.; He, S. High-Fidelity Model for Interior Permanent Magnet Synchronous Machines Considering the Magnet Saturation and Spatial Harmonics Based on Deep Neural Network. In Proceedings of the 22nd International Conference on Electrical Machines and Systems (ICEMS), Harbin, China, 11–14 August 2019; pp. 1–5. [[CrossRef](#)]
16. Gebregergis, A.; Chowdhury, M.H.; Islam, M.S.; Sebastian, T. Modeling of Permanent-Magnet Synchronous Machine Including Torque Ripple Effects. *IEEE Trans. Ind. Appl.* **2014**, *51*, 232–239. [[CrossRef](#)]
17. Herold, T.; Franck, D.; Lange, E.; Hameyer, K. Extension of a d-q model of a permanent magnet excited synchronous machine by including saturation, cross-coupling and slotting effects. In Proceedings of the 2011 IEEE International Electric Machines and Drives Conference, IEMDC 2011, Niagara Falls, ON, Canada, 15–18 May 2011; pp. 1363–1367. [[CrossRef](#)]
18. Bianchi, N.; Alberti, L. MMF Harmonics Effect on the Embedded FE Analytical Computation of PM Motors. *IEEE Trans. Ind. Appl.* **2010**, *46*, 812–820. [[CrossRef](#)]
19. Xu, L.; Zhang, C.; Zhu, X.; Lin, M.; Zheng, S. Indirect Analytical Modeling and Analysis of V-Shaped Interior PM Synchronous Machine. *IEEE Access* **2019**, *7*, 173786–173795. [[CrossRef](#)]
20. Lee, J.; Kwon, Y.-C.; Sul, S.-K. Identification of IPMSM Flux-Linkage Map for High-Accuracy Simulation of IPMSM Drives. *IEEE Trans. Power Electron.* **2021**, *36*, 14257–14266. [[CrossRef](#)]
21. Sano, H.; Narita, K.; Asanuma, T.; Yamada, T. An accurate iron loss evaluation method based on finite element analysis for permanent magnet motors. In Proceedings of the 2016 XXII International Conference on Electrical Machines (ICEM), ICEM 2016, Lausanne, Switzerland, 4–7 September 2016; pp. 1284–1289.
22. Ruuskanen, V.; Nerg, J.; Rilla, M.; Pyrhonen, J. Iron Loss Analysis of the Permanent-Magnet Synchronous Machine Based on Finite-Element Analysis Over the Electrical Vehicle Drive Cycle. *IEEE Trans. Ind. Electron.* **2016**, *63*, 4129–4136. [[CrossRef](#)]
23. Duck, P.; Ponick, B. A novel iron-loss-model for permanent magnet synchronous machines in traction applications. In Proceedings of the 2016 International Conference on Electrical Systems for Aircraft, Railway, Ship Propulsion and Road Vehicles & International Transportation Electrification Conference (ESARS-ITEC), Toulouse, France, 2–4 November 2017; pp. 1–6. [[CrossRef](#)]
24. Zhu, S.; Cheng, M.; Dong, J.; Du, J. Core Loss Analysis and Calculation of Stator Permanent-Magnet Machine Considering DC-Biased Magnetic Induction. *IEEE Trans. Ind. Electron.* **2014**, *61*, 5203–5212. [[CrossRef](#)]
25. Lee, J.; Nam, K.; Choi, S.; Kwon, S. Loss-Minimizing Control of PMSM with the Use of Polynomial Approximations. *IEEE Trans. Power Electron.* **2009**, *24*, 1071–1082. [[CrossRef](#)]
26. Fernandez-Bernal, F.; Garcia-Cerrada, A.; Faure, R. Determination of parameters in interior permanent-magnet synchronous motors with iron losses without torque measurement. *IEEE Trans. Ind. Appl.* **2001**, *37*, 1265–1272. [[CrossRef](#)]
27. Zhang, Z.; Liu, X. A Duty Ratio Control Strategy to Reduce Both Torque and Flux Ripples of DTC for Permanent Magnet Synchronous Machines. *IEEE Access* **2019**, *7*, 11820–11828. [[CrossRef](#)]
28. Wang, H.; Li, C.; Zhang, G.; Geng, Q.; Shi, T. Maximum Torque Per Ampere (MTPA) Control of IPMSM Systems Based on Controller Parameters Self-Modification. *IEEE Trans. Veh. Technol.* **2020**, *69*, 2613–2620. [[CrossRef](#)]
29. Balamurali, A.; Feng, G.; Kundu, A.; Dhulipati, H.; Kar, N.C. Noninvasive and Improved Torque and Efficiency Calculation Toward Current Advance Angle Determination for Maximum Efficiency Control of PMSM. *IEEE Trans. Transp. Electrification* **2019**, *6*, 28–40. [[CrossRef](#)]
30. Elsherbiny, H.; Ahmed, M.K.; Elwany, M.A. Online efficiency optimization of IPMSM for electric vehicles. *Int. J. Power Electron. Drive Syst. (IJPEDS)* **2021**, *12*, 1369–1378. [[CrossRef](#)]
31. You, Y.-M. Optimal Design of PMSM Based on Automated Finite Element Analysis and Metamodeling. *Energies* **2019**, *12*, 4673. [[CrossRef](#)]
32. Chen, X.; Wang, J.; Sen, B.; Lazari, P.; Sun, T. A High-Fidelity and Computationally Efficient Model for Interior Permanent-Magnet Machines Considering the Magnetic Saturation, Spatial Harmonics, and Iron Loss Effect. *IEEE Trans. Ind. Electron.* **2015**, *62*, 4044–4055. [[CrossRef](#)]
33. Sadeghi, S.; Milimonfared, J.; Mirsalim, M. Dynamic modeling and simulation of a series hybrid electric vehicle using a switched reluctance motor. In Proceedings of the 2007 International Conference on Electrical Machines and Systems (ICEMS), Seoul, Korea, 8–11 October 2007; pp. 2017–2022. [[CrossRef](#)]

-
34. Lin, D.; Zhou, P.; Fu, W.; Badics, Z.; Cendes, Z. A Dynamic Core Loss Model for Soft Ferromagnetic and Power Ferrite Materials in Transient Finite Element Analysis. *IEEE Trans. Magn.* **2004**, *40*, 1318–1321. [[CrossRef](#)]
 35. Liu, G.; Liu, M.; Zhang, Y.; Wang, H.; Gerada, C. High-Speed Permanent Magnet Synchronous Motor Iron Loss Calculation Method Considering Multiphysics Factors. *IEEE Trans. Ind. Electron.* **2019**, *67*, 5360–5368. [[CrossRef](#)]